JOURNAL OF THE MECHANICAL BEHAVIOR OF BIOMEDICAL MATERIALS 20 (2013) 363–375

Available online at www.sciencedirect.com

SciVerse ScienceDirect

www.elsevier.com/locate/jmbbm


Research Paper

# Anisotropic behaviour of human gallbladder walls

W.G. Li[a,*], N.A. Hill[a], R.W. Ogden[a], A. Smythe[b], A.W. Majeed[b], N. Bird[b], X.Y. Luo[a]

[a]School of Mathematics & Statistics, University of Glasgow, Glasgow G12 8QW, UK
[b]Academic Surgical Unit, Royal Hallamshire Hospital, Sheffield S10 2JF, UK

ARTICLE INFO

*Article history:*
Received 23 November 2012
Received in revised form
11 February 2013
Accepted 20 February 2013
Available online 1 March 2013

*Keywords:*
Gallbladder
Emptying
Strain energy function
Nonlinear analysis
Fibre reinforced material
Constitutive equation
Inverse approach
Ultrasound images

ABSTRACT

Inverse estimation of biomechanical parameters of soft tissues from non-invasive measurements has clinical significance in patient-specific modelling and disease diagnosis. In this paper, we propose a fully nonlinear approach to estimate the mechanical properties of the human gallbladder wall muscles from in vivo ultrasound images. The iteration method consists of a forward approach, in which the constitutive equation is based on a modified Hozapfel–Gasser–Ogden law initially developed for arteries. Five constitutive parameters describing the two orthogonal families of fibres and the matrix material are determined by comparing the computed displacements with medical images. The optimisation process is carried out using the MATLAB toolbox, a Python code, and the ABAQUS solver. The proposed method is validated with published artery data and subsequently applied to ten human gallbladder samples. Results show that the human gallbladder wall is anisotropic during the passive refilling phase, and that the peak stress is 1.6 times greater than that calculated using linear mechanics. This discrepancy arises because the wall thickness reduces by 1.6 times during the deformation, which is not predicted by conventional linear elasticity. If the change of wall thickness is accounted for, then the linear model can used to predict the gallbladder stress and its correlation with pain. This work provides further understanding of the nonlinear characteristics of human gallbladder.



## 1. Introduction

The human gallbladder (GB) is a pressurised and pear-shaped elastic balloon that attaches to a lobe of the liver, and is connected to the liver and duodenum (small intestine). During normal fasting, the GB is relaxed, and it accommodates and concentrates the bile secreted by hepatocytes (Erlinger, 1992). The bile streams into the GB via the hepatic and cystic ducts because the sphincter of Oddi in the duodenum wall is closed. This phase is also known as the refilling process. Upon consumption of food or drinks, bile is expelled from the GB into the duodenum through the cystic and common bile ducts under rhythmic contraction of the GB and relaxation of the sphincter of Oddi. These contractions are stimulated by a chemical called hormonal cholecystokinin (CCK), which also helps digestion of food in the small intestine (Behar and Biancani, 1980; Mawe, 1998). This process is the emptying phase.

Acalculous biliary pain is a symptom of patients who suffer from significant abnormal pain in the absence of cholelithiasis (Michail et al., 2001). The pathogenesis of such disorders is not fully understood (Parkman et al., 1999). Many researchers believe that it is related to mechanical responses

*Corresponding author. Tel.: +44 141 330 4572.
E-mail address: Wenguang.Li@Glasgow.ac.uk (W.G. Li).

1751-6161/$ - see front matter © 2013 Elsevier Ltd. All rights reserved.
http://dx.doi.org/10.1016/j.jmbbm.2013.02.015

triggered by smooth muscle contraction of the GB (Smythe et al., 1998; Parkman et al., 1999; Wegstapel et al., 1999; Amaral et al., 2001; Merg et al., 2002). The mechanical behaviour of the human GB has been extensively studied, primarily using a linear membrane ellipsoid model (Liao et al., 2004; Li et al., 2008; Li et al., 2011a; Li et al., 2011b). However, to estimate the mechanical stress more accurately, it is necessary to consider the nonlinear material properties of the GB wall. Indeed, the nonlinear behaviour is shown in guinea-pig gallbladders (Ryan and Cohen, 1976; Bertuzzi et al,. 1992). The work of Bertuzzi et al. (1992) further showed that such an effect can be significant in gallbladder wall. In addition to nonlinearity, our recent work suggests that the human GB wall exhibits anisotropic behaviour (Li et al., 2012).

A particular challenge in human GB modelling is the estimation of the patient-specific material properties. As in many other applications, measurements of human tissue elasticity can be used to indicate pathological changes caused by disease, in e.g. carcinoma of the breast (Tilleman et al., 2004), plaque (Schulze-Bauer and Holzapfel, 2003; Karimi et al., 2008) and aging problems (Escoffier et al., 1989; Lee et al., 2010). Elastography, which evaluates mechanical properties of bio-tissue from medical images, is becoming an increasingly researched topic, since it has potential applications in clinical diagnoses (Samani and Plewes, 2007).

In many elastography studies one estimates either the elastic moduli (Guo et al., 2010), or a general linear elasticity tensor (Raghupathy and Barocas, 2010) directly by solving the equilibrium equations iteratively. Normally this requires solving direct linear problems repeatedly with successively updated material parameters. The computed strain or displacement field is then matched to experimental observations or medical images. For linear materials, the inverse problem is relatively easy to solve. The mechanical properties, e.g. Young's modulus (Guo et al., 2010) or a general linear elasticity tensor (Raghupathy and Barocas, 2010), can be determined directly from the force equilibrium equation iteratively (Moulton et al., 1995; Govindjee and Mihalic, 1998; Kauer et al., 2002; Seshaiyer and Humphrey, 2003; Bosisio et al., 2007; Lei and Szeri, 2007; Samani and Plewes, 2007; Gokhale et al., 2008; Karimi et al., 2008; Li et al., 2009; Balocco et al., 2010; Kroon, 2010).

For a finite-strain nonlinear problem, however, solving the inverse problem is much harder, because a challenging forward problem needs to be solved from an often unknown reference (zero-stress) configuration. In the previous studies where the mechanical properties are known, a zero-pressure state, which is often used to approximate the zero-stress configuration, can be determined from the loaded configuration (Govindjee and Mihalic, 1996; Govindjee and Mihalic, 1998; Raghavan et al., 2006; De Putter et al., 2007; Lu et al., 2007a; Lu et al., 2007b; Gee et al., 2009; Kroon, 2010; Vavourakis et al., 2011). However, in our problem, both the zero-stress configuration and the mechanical properties are unknown; hence we estimate the zero-stress configuration from the experimental observations.

The wall structure is illustrated in the histological graph of human GB wall (Fig. 1). These layers are the adventitia, muscle, mucosa and epithelium. The muscular layer is composed of many bundles of smooth muscle cells, collagen fibres and elastin. The smooth muscle cells and collagen fibres contribute to the passive response in refilling, and the smooth muscle cells are responsible for generating active stresses. Fig. 1 shows that the two large smooth muscle bundles with collagen fibres together run almost orthogonal to each other in the muscle layer, where denser smooth muscle bundles run circumferentially and several isolated bundles are in the longitudinal direction. Such a feature has been confirmed by in vitro experiments in which the Young's modulus of human GB wall in the passive state was found to be orientation-dependent (Su, 2005).

In a previous paper, we used a quasi-linear elastography inverse approach to estimate GB tissue elasticity during the emptying phase. We conducted linear analyses on a series of configurations of human GBs determined by ultrasonographic routine scans during emptying (Smythe et al., 1998; Li et al., 2008). The transmural pressure in the GBs, which was estimated from measured volume changes (Li et al., 2008), was applied as the loading condition. The mechanical property constants were determined so that the computed displacements at several observation points were adjusted against those from clinical measurements with the errors minimised in the least-squares sense.

In the present paper, for the GB muscle behaviour we employ a finite-strain fully nonlinear fibre-reinforced mechanical model based on the work of Holzapfel et al. (2000). The patient specific constitutive constants are inversely determined from a series of ultrasonic photography

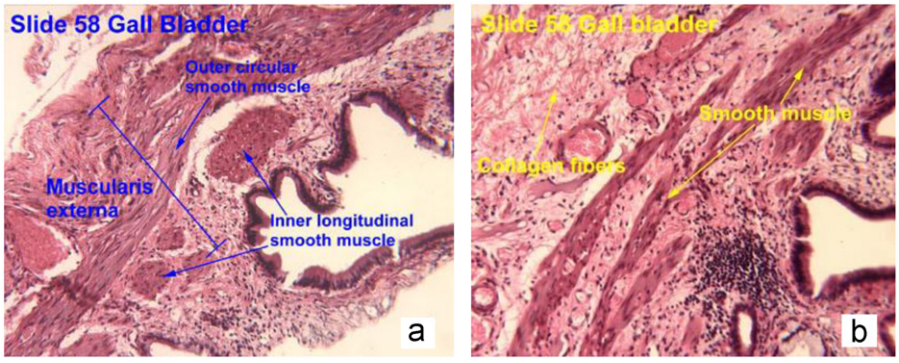


**Fig. 1 – The structure of human GB wall, where two families of orthogonal fibres are shown in the circumferential and longitudinal directions (image taken from 〈http://www.ouhsc.edu/histology/Glass%20slides/58_08.jpg〉).**

images during emptying (Smythe et al., 1998) using the FEM package ABAQUS, MATLAB and a Python code. To avoid modelling the active stress caused by smooth muscle cross-bridge phosphorylation during the emptying phase (Hai and Murphy, 1988a; Hai and Murphy, 1988b; Li et al., 2011b), here the inverse computations are carried out in the refilling phase where only the passive stress is involved.

## 2. Model and method

### 2.1. CCK provocation test and problem specification

CCK provocation tests were carried out on patients who had experienced repeated attacks of biliary pain in the absence of gallstones (Cozzolino et al., 1963). After an overnight fast, the patients were injected with an intravenous infusion of saline (control) followed by an intravenous infusion of CCK (0.05 μg/kg body weight). Ultrasonography of their GBs was taken to monitor initial volume, changes in shape, and volume as well as wall thickness at 5 or 15 min intervals for 60 min. The test was only considered positive when the patients' usual 'gall-bladder' pain was reproduced following CCK infusion (Smythe et al., 1998).

Fig. 2 shows schematically a pressure–volume diagram in the CCK provocation test. At point D, the sphincter of Oddi is closed, the patient is fasting, and the GB cavity volume and pressure are at their minimum levels. Between D and A, a low but positive pressure difference between the liver and the GB exists (Herring and Simpson, 1907), and hepatic bile is secreted slowly into the GB. During this refilling, the GB volume and pressure increase, and the smooth muscle in GB wall is passively stretched. At the point A, CCK starts to be infused, causing the GB to contract. The pressure in the GB rises rapidly up to point B in 3 to 10 min, and exceeds the pressure in the common bile duct. During this time, the sphincter of Oddi relaxes and the pressure in the common bile duct is lowered. The pressure in the GB is now much higher than in the common bile duct, and the emptying starts until the volume drops to $V_C$=(30~50)% $V_A$ (point C), and $p_C=p_A$. From point C to D, the GB wall is in isometric relaxation, with the pressure reduced from $p_C$ to $p_D$. The cycle is then repeated.

In the refilling phase, the GB wall is subject to a passive stretch. For simplicity, we assume the GB has the same shape at a given volume, regardless of whether it is in the refilling or emptying phase, as indicated in Fig. 2. This allows us to use the ultrasound images taken during emptying. We further assume that the pressure increases exponentially from $p_D$ to $p_A$ as a function of time, following Li et al. (2008).

### 2.2. The zero-stress configuration and the loading pressure

The human GB is simplified to an ellipsoid with a constant thickness as shown in Fig. 3(a). The axes of the ellipsoid are determined from the ultrasound images (Li et al., 2011a). Inspired by the image of the GB wall in Fig.1, we let two families of fibres be oriented in the circumferential and longitudinal directions, as shown in Fig. 3(b).

In order to examine the human GB stress-free configuration, two digital photos were taken against a GB, which was excised from a patient with gallstones, when it was full of bile and then after the bile was emptied completely (zero-pressure), as shown in Fig. 4. By noting the length between the mark and the apex of the GB fundus as well as the width of the fundus based on the scale in the photos, and assuming the GB is ellipsoidal with a thickness of 2.5 mm, it was found that the GB size shrunk by 50.6% after it was emptied, implying that the volume of zero-pressure configuration is around 50% of the filled GB, i.e. $V_C=V_D\approx 50\%\ V_A$ in Fig. 2. This zero-pressure configuration is also found to be approximately stress-free since no opening angles were detected after longitudinal or circumferential cuts were made on several GBs excised during cholestectomy.

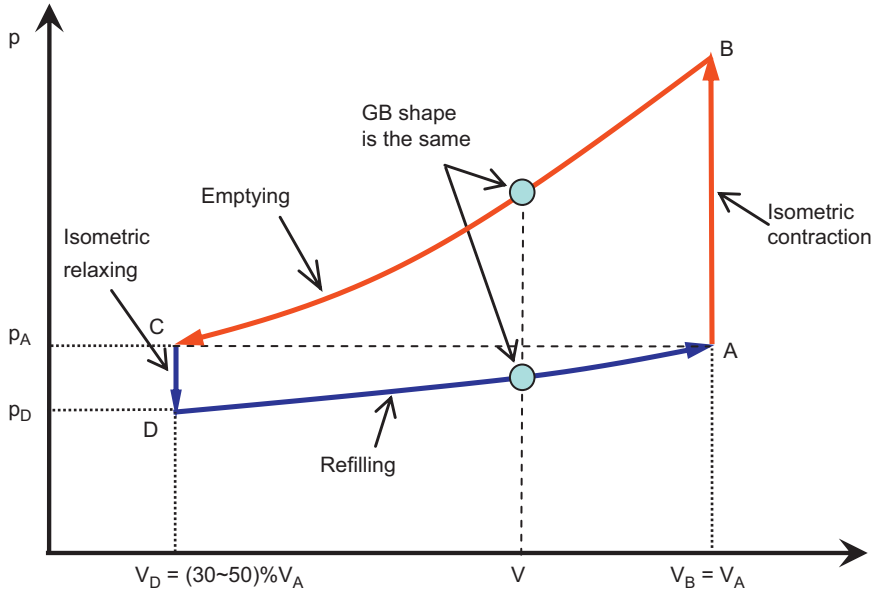


**Fig. 2 – Typical pressure–volume diagram of the GB during the CCK provocation test. Only passive refilling is modelled here.**

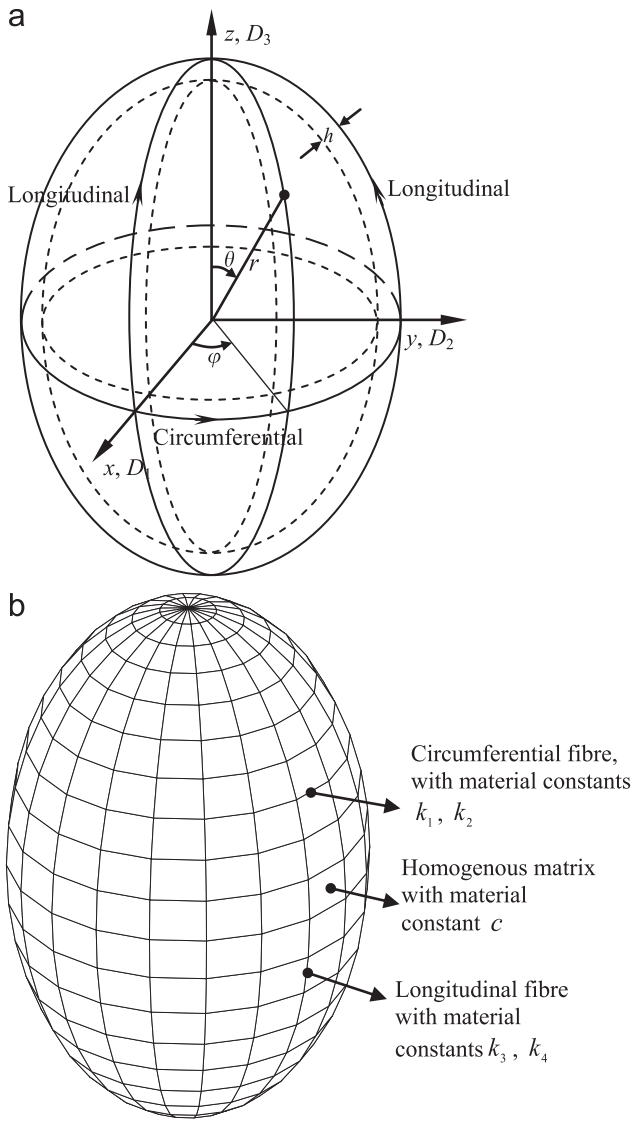


**Fig. 3 – (a) The ellipsoid shell model of human GB; (b) two families of orthogonal fibres are aligned in the longitudinal and circumferential directions.**

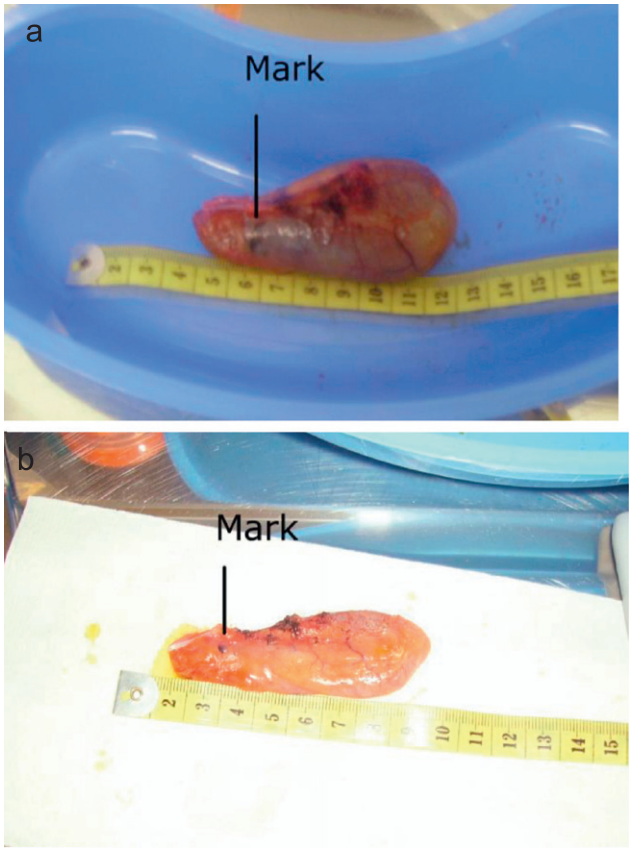


**Fig. 4 – Excised human GB with bile (a), and without bile (the zero-loading configuration) (b). A 50% decrease in volume is observed when bile is expelled from the GB.**

There are limited intraluminal pressure measurements in vivo in the human GB during passive refilling. However, GB pressure has been monitored in vivo in the guinea pigs when the animal suffered from dietary cholesterol and indomethacin caused from cholelithiasis, by means of an infusion/withdrawal pump, catheter and pressure transducer (Brotschi et al., 1984). The intraluminal pressure of human GB with acute cholcystitis was also measured in vivo (Borly et al., 1996). Based on this, in this paper, we choose the basal intraluminal GB pressure to be $p_D=3.5$ mmHg (466.6 Pa) (Borly et al., 1996), and $p_A=11$ mmHg (1466.5 Pa) (Li et al., 2008, 2011a).

The pressure inside the GB can be related to the volume change using the Windkessel model (Li et al., 2008; Westerhof et al., 2009):

$$\frac{dp}{dt}+\frac{p}{RC}=\frac{Q}{C}, \tag{1}$$

where C is the GB compliance, R is the downstream flow resistance, and Q is the flow rate into the GB. During the refilling, the flow rate is very slow, so can be approximated as zero, and integration of Eq. (1) gives

$$p=p_D\left(\frac{p_A}{p_D}\right)^{t/t_{DA}},\ t\in[0,t_{DA}], \tag{2}$$

where $t_{DA}$ is the total refilling time. The conditions $p=p_D$ at $t=0$, and $p=p_A$ at $t=t_{DA}$ are used in deriving Eq. (2).

### 2.3. *The constitutive model*

A general constitutive model was initially proposed by Humphrey and Yin (1987) for human soft tissues, based on a combination of existing phenomenological and micro-structural features. In their work, the human soft tissue is simplified to a mixture of a homogeneous matrix and a number of families of distributed thin extensible fibres, where the fibres and the matrix share the same gross deformation field. The total strain energy is the sum of the different strain energy functions of non-muscle matrix, non-linear straight elastin and wavy collagen fibres. For the walls of arteries, a simpler version was put forward by Holzapfel et al. (2000), where the elastin was part of the homogeneous, incompressible matrix material. The collagen is embedded in as fibre bundles with preferred orientations. The matrix material and collagen fibres have different strain energy

functions (Holzapfel et al. 2000) so that the total strain energy function is

$$\Psi = c(\bar{I}_1 - 3) + \frac{k_1}{2k_2}\sum_{i=4,6}[e^{k_2(\bar{I}_i-1)^2}-1], \tag{3}$$

where the first term represents the contribution of the matrix, whereas the last two denote the collagen effect. $c$ is the matrix material property constant, while $k_1$ and $k_2$ are the material constants for collagen. Note that in this model, the two families of fibres share the same mechanical properties. The invariants $\bar{I}_1$, $\bar{I}_4$ and $\bar{I}_6$ have the following forms (Holzapfel et al. 2000):

$$\begin{aligned}&\bar{I}_1 = tr(\bar{C}), I_4 = C_{ij}n_{4i}n_{4j}, \bar{I}_6 = \bar{C}_{ij}n_{6i}n_{6j}\\ &\bar{C} = J^{-2/3}\mathbf{C}, \mathbf{C} = (2\mathbf{E}+\mathbf{I})\\ &i = 1,2,3, j = 1,2,3\end{aligned} \tag{4}$$

where $\mathbf{C}$ is the Cauchy-Green deformation tensor, $\mathbf{C}=\mathbf{F}^T\mathbf{F}$, and $\mathbf{F}$ is the deformation tensor, $J=\det\mathbf{F}$. $n_{4i}$ (i=1,2,3) are the direction cosines for the first family of fibres, and $n_{6i}$ (i=1,2,3) are the direction cosines for the second family of fibres. $\bar{I}_4$ and $\bar{I}_6$ are the squared stretch ratios in the directions of the two families of fibres. $\mathbf{E}$ is the Green-Lagrange strain tensor, and $\mathbf{I}$ is a $3\times3$ identity tensor. Note that the GB wall is assumed to be incompressible, i.e. $J=1$ and the strain energy function due to the volumetric deformation is zero, i.e. $\Psi_{vol} = K\ln J/2 = 0$, where $K$ is the bulk modulus of the GB wall. Therefore the strain energy function in Eq. (3) represents isochoric deformation only.

The material parameters $c$, $k_1$ and $k_2$ are usually determined in vitro by mechanical experiment for special specimens, such as segments (Holzapfel and Weizsäcker, 1998; Holzapfel et al., 2000) or strips (Holzapfel et al., 2005a) of the aorta or the artery wall. A more recent investigation indicates the neo-Hookean strain energy function represented by the first term of Eq. (3) is able to capture the mechanical response of elastin (Watton et al., 2009).

We propose that the human GB wall is composed of homogeneous elastic matrix material and two families of collagen fibres and smooth muscle cells in the circumferential and the longitudinal directions. However, here we assume that each fibre family has different mechanical property constants (Fig. 3b), and hence the strain energy function is

$$\Psi = c(\bar{I}_1 - 3) + \frac{k_1}{2k_2}\left[e^{k_2(\bar{I}_4-1)^2}-1\right] + \frac{k_3}{2k_4}\left[e^{k_4(\bar{I}_6-1)^2}-1\right], \tag{5}$$

where the direction cosines $n_{4i}$, $n_{6i}$ of the two orthogonal families of fibres are determined from

$$\begin{aligned}&n_{41} = -\sin\varphi_C, n_{42} = \cos\varphi_C, n_{43} = 0\\ &n_{61} = \cos\theta_L\cos\varphi_L, n_{62} = \cos\theta_L\sin\varphi_L, n_{63} = -\sin\theta_L\end{aligned}. \tag{6}$$

in which $\varphi_C$ is the azimuth angle of the circumferential family of fibres, and $\theta_L$ and $\varphi_L$ are the zenith and azimuth angles of the longitudinal family of fibres, respectively, as shown in Fig. 3(a). Because experimental information on smooth muscle cell response is lacking, in this model, the passive contribution from the smooth muscle cells is not separated from that of the collagen fibres. The last two terms in Eq.(5) present the combined contribution from smooth muscles and fibres.

The values of material parameters $c$, $k_1$, $k_2$, $k_3$ and $k_4$ are to be determined from the inverse approach.

### 2.4. The computational methods

The finite element model of each GB is generated using ABAQUS 6.11-2. A minimum of 6100 quadrilateral elements are used, and for each GB, the edge length is kept to be between 1–1.5 mm. We use the 4-node shell element with large-strain formulation which has excellent stability in the numerical solution procedure. In solving the inverse problem, we specify the constitutive model and the material parameters in a user-subroutine in the forward problem simulation.

The optimisation process is controlled using MATLAB. During each pressure-loading step, the objective function:

$$\begin{aligned}f(c,k_1,k_2,k_3,k_4) = \sum_{i=1}^{N}(&\left|\Delta D_1 - \Delta D_1^{exp}\right|_i + \left|\Delta D_2 - \Delta D_2^{exp}\right|_i\\ &+\left|\Delta D_3 - \Delta D_3^{exp}\right|_i)^2,\end{aligned} \tag{7}$$

is minimised. Here $N$ is the number of the pressure increments, chosen to be 15 here. $\Delta D_j$, $\Delta D_j^{exp}$, $j$=1–3, are the computed and measured peak displacements in the $x$, $y$ and $z$ directions, respectively.

In addition, we evaluate the volume error using

$$\varepsilon_V = \frac{1}{N}\sum_{i=1}^{N}\left|\frac{1}{6}\pi(D_1^0+\Delta D_1)_i(D_2^0+\Delta D_2)_i(D_3^0+\Delta D_3)_i - V_i^{exp}\right|/V_1^{exp} \tag{8}$$

where $D_j^0$, $j$=1–3, are the dimensions of GB at the zero-pressure loading, and $V_i^{exp}$ is the GB volume measured from images at the time $t_i$.

Each loop of the inverse analysis requires launching ABAQUS eight times, and a total of 10–20 loops of inverse analysis are needed to reduce the change of the objective function value in Eq. (7) to be below $10^{-3}$. The Trust–Region–Reflective algorithm of Moré and Sorensen (1983) is applied to minimise the objective function Eq. (7). The detailed procedure is shown in the flow chart in Fig. 5.

## 3. Validations

We first validate our approach using optical measurements for human arteries (Avril et al., 2010), and inversely estimating the material parameters $\beta$, $c$, $k_1$ and $k_2$ of the artery model. The dimensions of the zero-pressure configuration of the artery are shown in Fig. 6a. Following Avril et al. (2010), the experimental artery is treated as a membrane without residual stress, and with two spiral families of fibres, as shown in Fig. 6(a). The experimental internal pressure loading profile is plotted in terms of artificial time in Fig. 6(b). The length of the artificial time does not affect the computational results. All the displacements of the bottom of the artery are fixed to zero, and a 10% longitudinal strain and a zero radial displacement are applied at the top of the artery. The same Hozapfel–Gasser–Ogden (HGO) law, as specified by Eq. (3), is used as the constitutive model.

The estimated material parameters $\beta$, $c$, $k_1$ and $k_2$, as well as the peak radial displacement $\Delta R$ against internal pressure are illustrated in Fig. 6(c). The agreement between the model

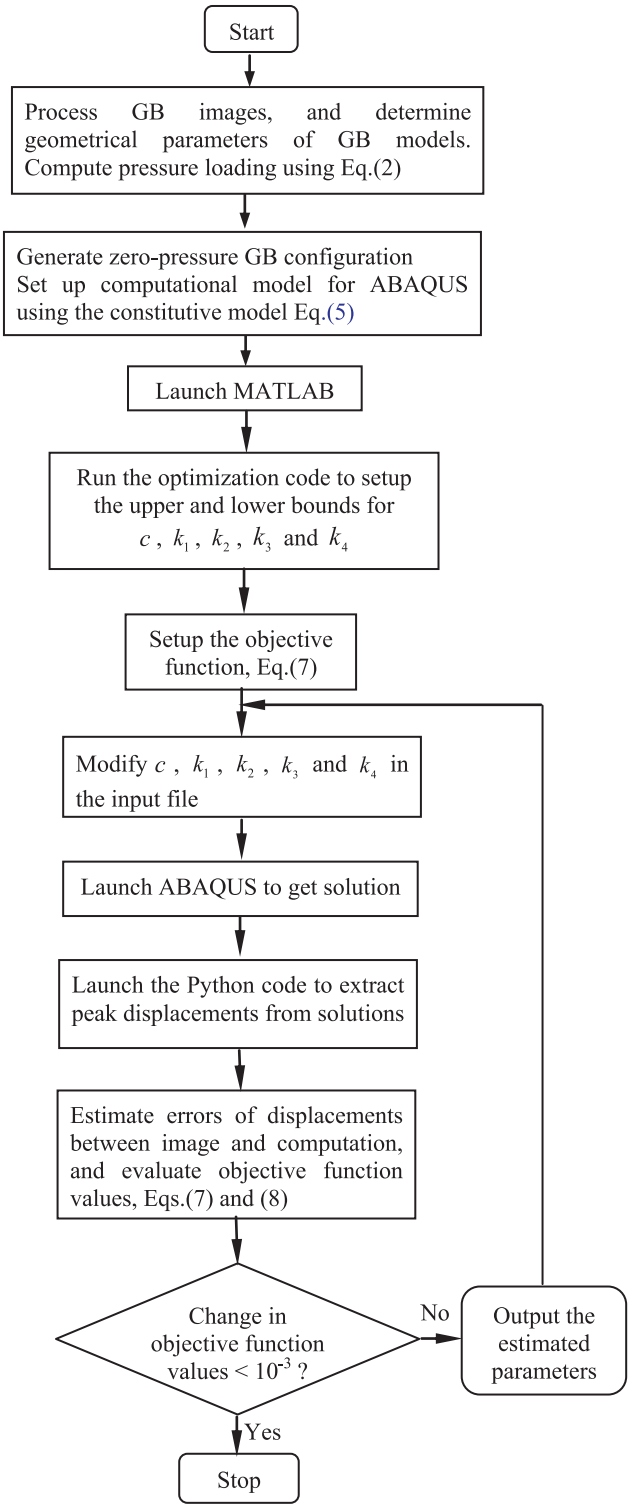


**Fig. 5 – Flow chart for the inverse method.**

prediction and the experimental data is very good with a maximum error of 2.03% in the peak radial displacement. For comparison, we also plotted the peak radial displacement computed using the Fung strain energy density function. Fig. 6(c) shows that the HGO model seems to give better agreement with the experimental measurements compared with the Fung model.

## 4. Results

### 4.1. *Model parameters*

Ten human GB models were chosen to investigate the nonlinear effect of the human gallbladder wall muscles. These GBs differ in size and emptying behaviour; see the detailed parameters listed in Table 1. For simplicity, a uniform wall thickness ($h$=2.5 mm in Fig. 3a) is assumed for all the models (Li et al., 2008). The ejection fraction (EF) recorded 30 min into the emptying phase is also shown in Table 1. A good emptying behaviour is usually accompanied by a good refilling activity, and this can be indicated by a greater value of EF or the larger peak longitudinal displacement.

### 4.2. *The material parameters*

The estimated material parameters of the ten GB models are tabulated in Table 2. These parameters change in the ranges of $c\in$[1.68, 2.94] kPa, $k_1\in$[0.60, 6.24] kPa, $k_2\in$[0.018, 1.36], $k_3\in$[0.15, 1.40] kPa and $k_4\in$[0.78, 1.55].

In general, the matrix material parameter $c$ shows little variation from one subject to another; however, the other parameters seem to be more patient-dependent. Moreover, most of the GB samples have stiffer circumferential fibres (indicated by a larger value of $k_1$) compared with the longitudinal ones (indicated by a smaller value of $k_3$), with the exception of GB1 (Table 1).

For comparison, we list the material parameters of the rabbit carotid artery in Table 3 obtained by Holzapfel et al. (2000) based on the experimental data of Fung et al. (1979). The material parameters of the human GB seem to be in similar ranges to those of the media of the rabbit carotid artery.

### 4.3. *Peak displacements*

The estimated peak displacements and the $p$–$V$ curves are shown in Fig. 7 for five of the GB samples. All the other samples exhibit similar patterns and are not shown. In particular, the $p$–$V$ curves in Fig. 7 show that the GB volume estimated from the modelling agrees very well with that of the images. Also, the peak displacement $\Delta D_3$ is consistent with the observations. However, there are some discrepancies in $\Delta D_1$ $\Delta D_2$, especially for GB1, 19, 21. These are presumably due to the simplification of using an ellipsoid model. While such a simplification is adopted clinically, it has been pointed out that the error between the actual image and an ellipsoid assumption is around 12.5% (Pauletzki et al., 1996).

We observe in Fig. 7 that there is a kink in each curve, which occurs at the second loading step. The reason for this is that that we chose our reference configuration to be the configuration when the GB is subject to a pressure 3.5 mmHg (beginning of the refilling), and ignored the initial stress in this configuration. If the parameter properties are known, one can in principle determine this initial stress. But we need to estimate the material properties in the first instance. As a result, the structure undergoes a significant displacement at

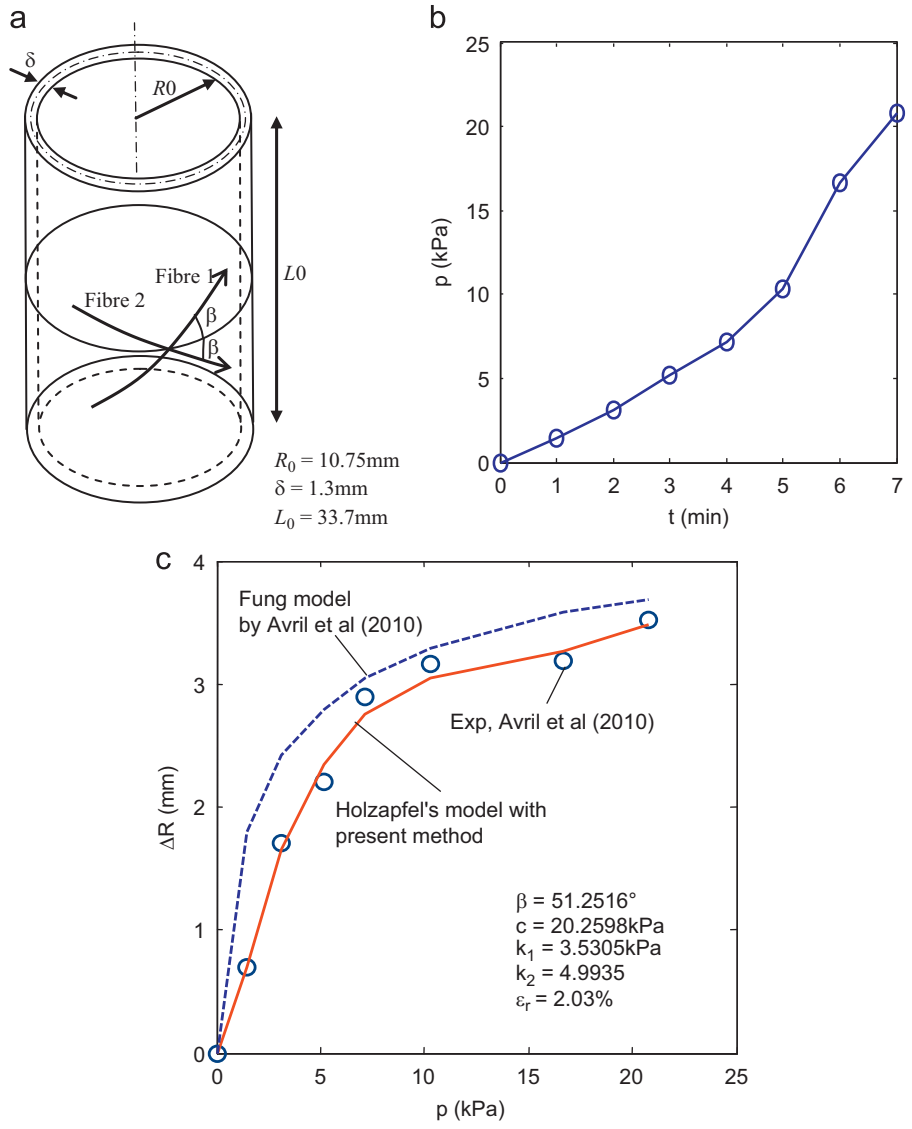


**Fig. 6 – (a) The artery geometry from Avril et al (2010), (b) internal pressure vs. time, and (c) comparison of the peak radial displacement against pressure; where the circles are the experimental data, the solid (red) curve is our result, and the dotted curve shows the results computed by Avril et al (2010) using the Fung strain energy function. (For interpretation of the references to color in this figure legend, the reader is referred to the web version of this article.)**

the second step of loading, giving rise to the kink. Therefore, results near this kink are not accurate.

### 4.4. *Stress field*

The contours of the peak 1st and 2nd principal stresses at the end of refilling in GB 37 are illustrated in Fig. 8. These are compared with the earlier results using a simplified linear membrane model, as well as with the incremental linear analysis (Li et al., 2012). The stress patterns of the present nonlinear model are similar to those of the linear model, but the maximum and minimum principal stresses of the nonlinear material are increased to about 1.67 times to those of the linear model. Similar results are found for other GB samples. The comparisons for all other GB samples are summarised in Table 5.

## 5. Discussion

Up to this point, we have assumed that there are two families of fibres with different stiffnesses. An alternative, perhaps more natural choice, would be to assume that all collagen fibres are of the same quality but their density may vary with orientation. If so, then $k_2=k_4$. By applying this constraint during the inverse procedure, we estimate and list the corresponding mechanical parameters in Table 4. This is to be compared with Table 2. It is clear that the parameter values (i.e. $c$, $k_1$ and $k_3$) are changed when imposing this constraint. However, the overall variation of the parameters with the sample numbers is still similar. Most importantly, the stress patterns under these two conditions are similar, as shown in Fig. 8, although the peak stress is slightly reduced, e.g. by about 2.2% for GB 37, when $k_2=k_4$.

**Table 1 – Parameters of the human GB samples.**

| | Parameter | Model GB No. | | | | | | | | | |
|---|---|---|---|---|---|---|---|---|---|---|---|
| | | 1 | 3 | 4 | 17 | 19 | 21 | 29 | 37 | 39 | 43 |
| At end of refilling | $p_A$(Pa) | 1466.5 | | | | | | | | | |
| | $D_1^A$(mm) | 23.4 | 26.8 | 32.9 | 27.2 | 34.7 | 28.2 | 28.1 | 30.2 | 33.2 | 37.6 |
| | $D_2^A$(mm) | 25.0 | 27.9 | 35.2 | 27.2 | 35.7 | 30.1 | 28.9 | 30.8 | 33.5 | 38.0 |
| | $D_3^A$(mm) | 54.1 | 70.7 | 57.5 | 55.9 | 92.3 | 74.5 | 56.1 | 53.8 | 53.9 | 82.1 |
| Zero loading configuration | $p_D$(Pa) | 466.6 | | | | | | | | | |
| | $D_1^D$(mm) | 16.8 | 21.0 | 24.8 | 21.4 | 26.8 | 20.8 | 20.1 | 24.7 | 24.2 | 28.1 |
| | $D_2^D$(mm) | 18.2 | 21.2 | 25.8 | 20.7 | 29.2 | 24.2 | 22.7 | 24.7 | 26.1 | 29.7 |
| | $D_3^D$(mm) | 51.7 | 59.3 | 54.9 | 46.7 | 72.9 | 62.9 | 49.9 | 41.2 | 47.5 | 70.3 |
| Peak displacement from images | $\Delta D_1^{exp}$(mm) | 6.6 | 5.8 | 7.5 | 5.8 | 7.9 | 4.0 | 8.0 | 5.8 | 9.0 | 9.5 |
| | $\Delta D_2^{exp}$(mm) | 6.8 | 6.6 | 7.7 | 6.5 | 6.5 | 9.3 | 6.2 | 5.8 | 7.4 | 8.3 |
| | $\Delta D_3^{exp}$(mm) | 2.4 | 11.4 | 10.0 | 9.2 | 19.4 | 11.6 | 6.2 | 12.6 | 6.4 | 11.8 |
| Ejection Fraction (EF) in 30 min (%) | | 4.5 | 11.4 | 13.3 | 32.4 | 49.4 | 66.3 | 37.8 | 77.0 | 60.1 | 2.7 |

**Table 2 – Material parameters inversely estimated for the GB samples.**

| GB | c(kPa) | $k_1$(kPa) | $k_2$ | $k_3$(kPa) | $k_4$ | $\varepsilon_V$(%) |
|---|---|---|---|---|---|---|
| 1 | 2.3349 | 0.5977 | 0.8512 | 1.3952 | 1.0430 | 2.2 |
| 3 | 1.8375 | 4.7385 | 1.3538 | 0.8694 | 0.9568 | 3.9 |
| 4 | 2.1817 | 2.9539 | 0.7230 | 0.6578 | 1.0458 | 3.0 |
| 17 | 1.6810 | 2.9213 | 0.1161 | 0.4784 | 1.5530 | 2.5 |
| 19 | 2.2772 | 6.2427 | 0.1106 | 0.2182 | 0.8042 | 3.0 |
| 21 | 2.2309 | 3.0375 | 0.0176 | 0.2213 | 0.7755 | 3.4 |
| 29 | 2.0624 | 1.6658 | 0.7148 | 0.8237 | 1.1547 | 2.6 |
| 37 | 1.9243 | 4.3563 | 0.4350 | 0.1451 | 1.3890 | 2.5 |
| 39 | 2.4066 | 1.7295 | 0.5803 | 0.8437 | 1.1167 | 2.5 |
| 43 | 2.9435 | 3.3794 | 0.0741 | 0.3327 | 1.0654 | 2.7 |

This suggests that a simpler model with parameters listed in

**Table 3 – Parameters of rabbit carotid artery estimated by (Holzapfel, Gasser et al, 2000).**

| Artery | β(°) | c(kPa) | $k_1$(kPa) | $k_2$ |
|---|---|---|---|---|
| Media | 29.0 | 3.0000 | 2.3632 | 0.8393 |
| Adventitia | 62.0 | 0.3000 | 0.5620 | 0.7112 |

Table 4 could be used to predict the stress pattern in the GB wall.

As the peak stress is found to be correlated to GB pain in our previous studies (Li et al. 2008, 2011a), it is important to obtain a reliable stress estimate based on routine clinical scans. The challenge is that, as in all the biological soft tissue modelling, the GB wall muscle obeys nonlinear anisotropic constitutive laws, with patient-specific material parameters that are not available from non-invasive measurements. Our earlier work shows that using a simple linear elasticity model, it is possible to predict the CCK induced GB pain with the success rate of over 76%. In this paper, we evaluate the stress in the GB model by improving our earlier simplified linear models. However, the stress evaluated in the more sophisticated nonlinear finite strain approach seems to be 1.67 times greater than the corresponding linear model (Table 5 and Fig. 8(c)).

The same effect of the zero-pressure configuration on stress estimates of human carotid atherosclerotic plaque or AAA has been reported by other groups (De Putter et al., 2007; Huang et al., 2009; Speelman et al., 2009). For example, if the current configuration of the artery is shrunk by 25% and 7.9% in the axial and circumferential directions in order to mimic its zero-pressure configuration, the maximum principal stress and strain is found to increase by 249.8% and 149% under an axial stretching of 1.33 (Huang et al., 2009).

If the linear modelling underestimates the stress level in the GB wall, then how do we explain the seemly good correlation between the "pain" predicted by the linear model (here pain is defined as when the peak stress is over a stress threshold) and the clinical observation (Li et al., 2011a). Further inspection shows that the "stress threshold" used is evaluated from the pressure threshold measured on common bile duct inflation by saline (Gaensler, 1951), and a linear model (Case et al., 1999) is used to estimate the stress from the recorded pressure of the common bile duct. Hence the same degree of the underestimate of the "experimental measure" of the threshold is introduced.

To illustrate this important point, we consider the experimental data recorded when changed configurations are taken into consideration for pig common bile duct (Duch et al., 2004). A linear model for the hoop stress gives (Case et al., 1999)

$$\sigma_\theta = \frac{pd_0}{2h_0}, \tag{9}$$

where $p$ is the pressure in a common bile duct (kPa), and $d_0$=7.6 mm and $h_0$=1 mm are the diameter and thickness of the common bile duct at the zero-pressure loading (Duch et al., 2004) respectively. In linear elasticity, the stress–pressure relationship is completely described by Eq.(9). However, in the nonlinear finite strain modelling, both the diameter and wall thickness change with pressure (Duch et al., 2004), and the stress should be estimated using the changed (current) configuration, i.e.

$$\sigma_\theta = \frac{pd}{2h}. \tag{10}$$

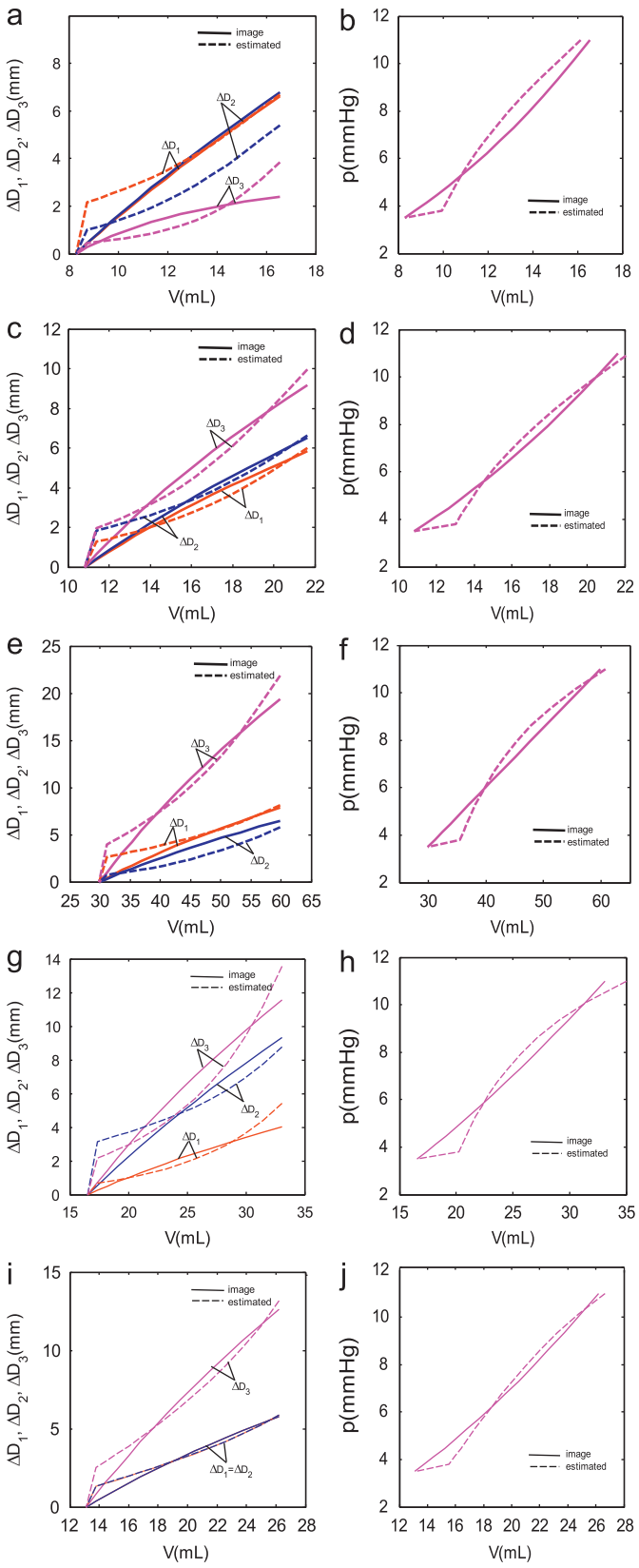


**Fig. 7 – Comparisons of the peak displacements and the GB volume estimated from the computational model and the clinical images for all GB samples. (a) GB1, (b) GB1, (c) GB17, (d) GB17, (e) GB19, (f) GB19, (g) GB21, (h) GB21, (i) GB37, (j) GB37.**

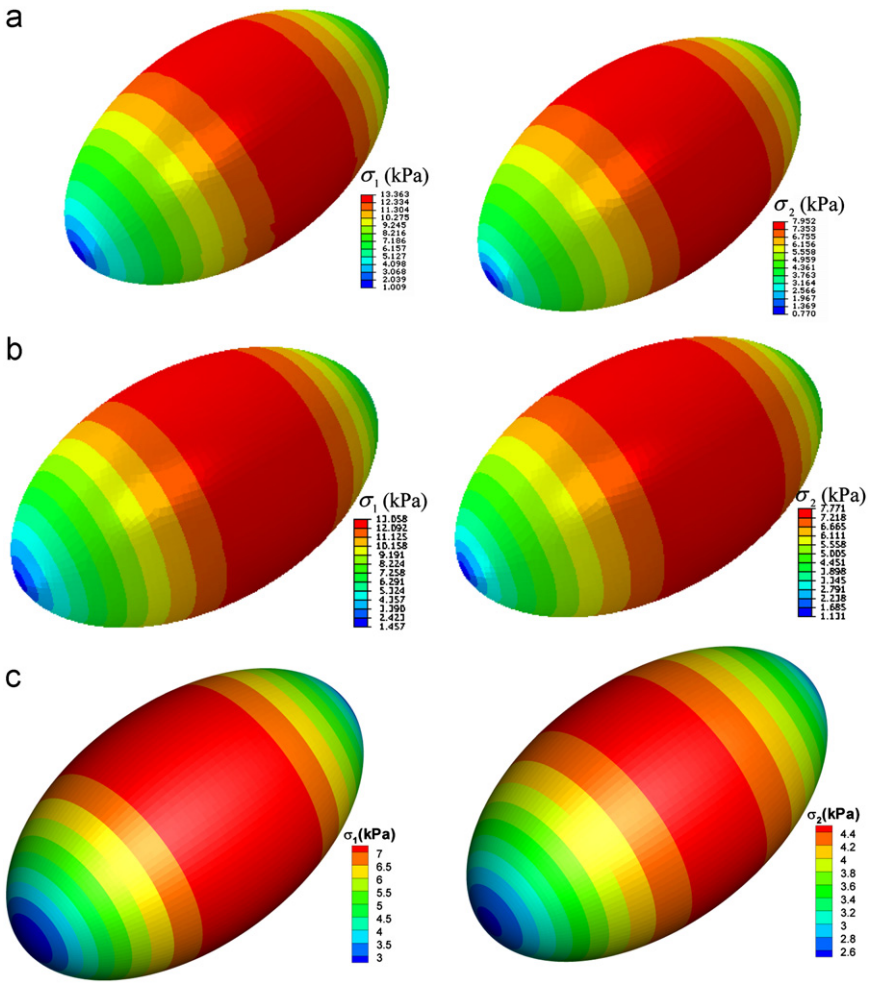


**Fig. 8 – Contours of the first and second principal stresses for GB37: (a) the present model, when $k_2 \neq k_4$, (b) the present model, when $k_2 = k_4$, and (c) results from the linear model by Li et al. (2011a). The stresses in (a) and (b) are very similar, except that the maximum principal stresses are reduced by about 2.2% if $k_2 = k_4$, but differ significantly in value from (c).**

This stress–pressure relation is plotted in Fig. 9, and compared with the results for the linear model Eq. (9). It is evident that the stress estimated by Eq. (9) is less than that of Eq. (10). Indeed, at the peak pressure (5 kPa or 37.4 mmHg), the ratio of the nonlinear to linear stress is 1.57. This is consistent with the ratios we obtained in Table 5. Importantly, Table 5 indicates that all ten GB models showed the same level of stress elevation using the nonlinear model, thus tentatively suggesting that the overall trend of the peak stress is captured using the linear model. This is presumably the reason for the good correlations between the linear stress and "linearly estimated stress threshold for pain" observed by Li et al. (2011a).

We further demonstrate that the increase in the magnitude of the stress is due to the change of wall thickness during the nonlinear analysis. At the end of the refilling, the thickness of the GB wall is reduced from its initial value of 2.5 mm to around 1.4–1.6 mm. This significant change of wall deformation is not captured by the linear model (Li et al., 2011a). If, however, we use the reduced wall thickness in the linear model, then the final stress from the linear model agrees with the nonlinear model. This is clearly illustrated in the bottom row of Table 5.

In Table 5, $\lambda_1$ and $\lambda_2$ are the first and second principal in-plane stretch ratios, $h = 2.5$ mm is the initial GB wall thickness. $1/(\lambda_1\lambda_2)(=\lambda_3)$ is the stretch ratio of the thickness and $h'^N = h/(\lambda_1\lambda_2)$ is the final thickness of GB wall at the end of refilling. Note here we made use of the incompressibility condition, $\lambda_1\lambda_2\lambda_3 = 1$. Since the GB size and shape are nearly the same for the both models, the reduced thickness in GB wall must be responsible for the increase in the magnitude of the stress.

Finally, we comment that in this paper the GB wall is assumed to be homogeneous because again we do not have experimental data to determine the inhomogeneous material properties, we only have non-invasive medical images. The more complicated the model, the harder it is to estimate the material properties. Given that the gallbladder wall is very thin, and that clinically it has been assumed to be a linear elastic balloon that is subject to Laplace's law, this study represents a new step in GB wall modelling by considering the nonlinear finite strain and fibre reinforced material properties. The fact that the model yields a good agreement with the imaged data suggests that the homogeneous assumption adopted here is acceptable.

The inverse nonlinear analysis approach has provided us with more insight into the stress–strain relations and the

material parameters. However, this approach is considerably more complicated and time consuming compared with the linear approach, and is impractical to apply to large cohort of GB samples. In addition, direct comparison with in vitro tensile experiments is much more difficulty due to lack of experimental data. The nonlinear modelling itself also still faces the same challenges as the linear model, namely, how to estimate the intraluminal pressure non-invasively, and how to evaluate the effects of patient specific GB geometries. In view of this, it seems plausible to continue to use the linear model as a clinical tool to provide a quick first evaluation of the stress trend, as has been done successfully in the previous studies (Luo et al., 2007; Li et al., 2011a, 2011b), but bear in mind that the stress within the GB wall may be underestimated by a factor of approximately 1.6, which reflects the ratio of the wall thickness reduction. However, for clinical cases that require careful attention and critical decision making, finite strain nonlinear models must be used to provide more accurate stress evaluations.

## 6. Conclusions

A finite strain nonlinear approach is developed to estimate the material parameters of human GB walls from routine non-invasive clinical ultrasound images. The human GB wall is modelled as a fibre-reinforced nonlinear material using a modified HGO constitutive law. The material parameters are estimated inversely with the forward problem solved using ABAQUS. The method proposed is validated with a published arterial model, and is subsequently used to analyse ten human GBs during refilling. It was demonstrated that the human GB wall is anisotropic. The material parameters are patient-specific. When compared with earlier linear models, we found there is a 60% increase in the maximum stress level. However, we demonstrate that such a discrepancy is due to applying the linear theory to large nonlinear deformation of biological tissues. Importantly, we found that if the deformed configuration is used, i.e. if the deformed wall thickness reduction is considered, then the linear model gives results consistent with those predicted by the nonlinear model. Since the nonlinear modelling is much more expensive with requirements for more patient-specific parameters and the zero-loading configuration, it seems that the simpler linear model could continue to be used with caution.

**Table 4 – Material parameters inversely estimated for the GB samples if $k_2=k_4$.**

| GB | c(kPa) | $k_1$(kPa) | $k_2=k_4$ | $k_3$(kPa) | $\varepsilon_V$(%) |
|---|---|---|---|---|---|
| 1 | 2.2923 | 0.7274 | 0.4251 | 1.8183 | 3.6 |
| 3 | 1.9750 | 4.8187 | 0.9086 | 0.6619 | 3.6 |
| 4 | 2.1930 | 2.9040 | 0.7720 | 0.6623 | 2.9 |
| 17 | 1.6901 | 2.5200 | 0.6251 | 0.5537 | 2.5 |
| 19 | 2.2187 | 5.9592 | 0.3933 | 0.3483 | 3.1 |
| 21 | 1.9108 | 3.1405 | 0.7274 | 0.6937 | 3.7 |
| 29 | 2.1800 | 2.0213 | 0.0234 | 0.8148 | 3.3 |
| 37 | 1.9524 | 4.0579 | 0.9358 | 0.1326 | 2.6 |
| 39 | 2.4542 | 1.8046 | 0.4772 | 0.8539 | 2.6 |
| 43 | 2.9539 | 3.0274 | 0.3583 | 0.4368 | 2.7 |

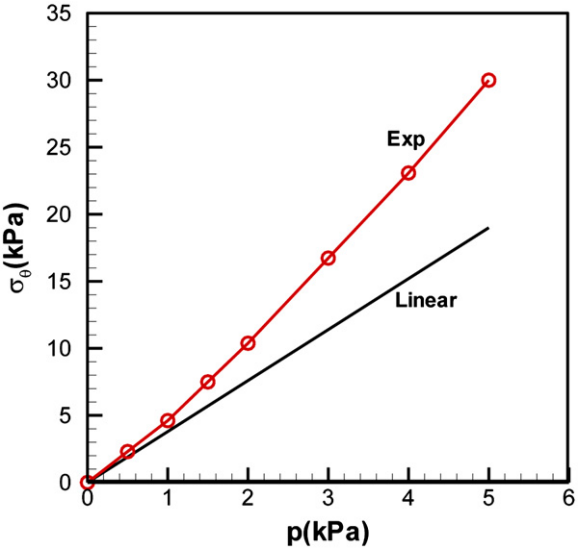


**Fig. 9 – The hoop stress vs the internal pressure, estimated from the experiment by Duch et al. (2004). The solid (red) line with circle is the stress estimated using the finite strain analysis, and the solid (black) line is from the linear analysis. (For interpretation of the references to color in this figure legend, the reader is referred to the web version of this article.)**

**Table 5 – The maximum peak first principal stress $\sigma_1$: linear vs nonlinear estimates.**

| Peak stress and thickness | GB No. | | | | | | | | | |
|---|---|---|---|---|---|---|---|---|---|---|
| | 1 | 3 | 4 | 17 | 19 | 21 | 29 | 37 | 39 | 43 |
| Present model, $\sigma_1$(kPa) | 9.75 | 12.38 | 13.66 | 11.89 | 17.11 | 14.41 | 12.17 | 12.78 | 13.26 | 17.09 |
| $\lambda_1 \times \lambda_2$ | 1.54 | 1.54 | 1.64 | 1.69 | 1.79 | 1.78 | 1.65 | 1.72 | 1.67 | 1.73 |
| Deformed wall thickness $h'=h/(\lambda_1 \times \lambda_2)$(mm) | 1.62 | 1.62 | 1.52 | 1.48 | 1.40 | 1.40 | 1.51 | 1.46 | 1.49 | 1.44 |
| Linear $\sigma_1^*$(kPa) using $h$=2.5mm , | 6.63 | 7.58 | 8.54 | 7.05 | 9.74 | 8.19 | 7.39 | 7.53 | 7.95 | 9.97 |
| The stress ratio,$\sigma_1/\sigma_1^*$ | 1.47 | 1.63 | 1.60 | 1.69 | 1.76 | 1.76 | 1.65 | 1.67 | 1.67 | 1.72 |
| Linear $\sigma'_1$(kPa) using $h'$ | 10.21 | 11.69 | 14.01 | 11.91 | 17.43 | 14.58 | 12.19 | 12.95 | 13.31 | 17.20 |

## Acknowledgements

The project is supported by EPSRC (Grant no. EP/G015651 and EP/G028257).

## REFERENCES

Amaral, J., Xiao, Z.L., Chen, Q., Yu, P., Biancani, P., Behar, J., 2001. Gallbladder muscle dysfunction in patients with chronic acalculous disease. Gastroenterology 120 (2), 506–511.

Avril, S., Badel, P., Duprey, A., 2010. Anisotropic and hyperelastic identification of in vitro human arteries from full-field optical measurements. Journal of Biomechanics 43 (15), 2978–2985.

Balocco, S., Camara, O., Vivas, E., Sola, T., Guimaraens, L., van Andel, H.A.F.G., Majoie, C.B., Pozo, J.M., Bijnens, B.H., Frangi, A.F., 2010. Feasibility of estimating regional mechanical properties of cerebral aneurysms in vivo. Medical Physics 37, 1689.

Behar, J., Biancani, P., 1980. Effect of cholecystokinin and the octapeptide of cholecystokinin on the feline sphincter of Oddi and gallbladder. Mechanisms of action. Journal of Clinical Investigation 66 (6), 1231.

Bertuzzi, A., A. Gandolfi, A.V. Greco, R. Mancinelli, G. Mingrone, S. Salinari, 1992. Material identification Of Guinea-pig gallbladder wall. The 14th Annual International Conference of the IEEE, Engineering in Medicine and Biology Society.

Borly, L., H½jgaard, L., Gr½nvall, S., Stage, J.G., 1996. Human gallbladder pressure and volume: validation of a new direct method for measurements of gallbladder pressure in patients with acute cholecystitis. Clinical Physiology 16 (2), 145–156.

Bosisio, M., Talmant, M., Skalli, W., Laugier, P., Mitton, D., 2007. Apparent Young's modulus of human radius using inverse finite-element method. Journal of Biomechanics 40 (9), 2022–2028.

Brotschi, E.A., Lamorte, W.W., Williams, L.F., 1984. Effect of dietary cholesterol and indomethacin on cholelithiasis and gallbladder motility in guinea pig. Digestive Diseases and Sciences 29 (11), 1050–1056.

Case, J., Chilver, L., Roos, C., 1999. Strength of Material and Structures. Arnold, London.

Cozzolino, H., Goldstein, F., Greening, R., Wirts, C., 1963. The cystic duct syndrome. Journal of the American Medical Association 185 (12), 920.

De Putter, S., Wolters, B., Rutten, M., Breeuwer, M., Gerritsen, F., Van De Vosse, F., 2007. Patient-specific initial wall stress in abdominal aortic aneurysms with a backward incremental method. Journal of Biomechanics 40 (5), 1081–1090.

Duch, B.U., Andersen, H., Gregersen, H., 2004. Mechanical properties of the porcine bile duct wall. Biomedical Engineering Online 3 (1), 23.

Erlinger, S., 1992. Bile secretion. British Medical Bulletin 48 (4), 860.

Escoffier, C., de Rigal, J., Rochefort, A., Vasselet, R., Lévêque, J.L., Agache, P.G., 1989. Age-related mechanical properties of human skin: an in vivo study. Journal of Investigative Dermatology 93 (3), 353–357.

Fung, Y., Fronek, K., Patitucci, P., 1979. Pseudoelasticity of arteries and the choice of its mathematical expression. American Journal of Physiology—Heart and Circulatory Physiology 237 (5), H620.

Gaensler, E., 1951. Quantitative determination of the visceral pain threshold in man. Journal of Clinical Investigations 30, 406.

Gee, M., Reeps, C., Eckstein, H., Wall, W., 2009. Prestressing in finite deformation abdominal aortic aneurysm simulation. Journal of Biomechanics 42 (11), 1732–1739.

Gokhale, N.H., Barbone, P.E., Oberai, A.A., 2008. Solution of the nonlinear elasticity imaging inverse problem: the compressible case. Inverse Problems 24, 045010.

Govindjee, S., Mihalic, P.A., 1996. Computational methods for inverse finite elastostatics. Computer Methods in Applied Mechanics and Engineering 136 (1–2), 47–57.

Govindjee, S., Mihalic, P.A., 1998. Computational methods for inverse deformations in quasi incompressible finite elasticity. International Journal for Numerical Methods in Engineering 43 (5), 821–838.

Guo, Z., You, S., Wan, X., Bicanic, N., 2010. A FEM-based direct method for material reconstruction inverse problem in soft tissue elastography. Computers and Structures 88 (23–24), 1459–1468.

Hai, C.M., Murphy, R.A., 1988a. Cross-bridge phosphorylation and regulation of latch state in smooth muscle. American Journal of Physiology—Cell Physiology 254 (1), 99–106.

Hai, C.M., Murphy, R.A., 1988b. Regulation of shortening velocity by cross-bridge phosphorylation in smooth muscle. American Journal of Physiology—Cell Physiology 255 (1), 86–94.

Herring, P., Simpson, S., 1907. The pressure of bile secretion and the mechanism of bile absorption in obstruction of the bile duct. Proceedings of the Royal Society of London. Series B, Containing Papers of a Biological Character 79 (535), 517–532.

Holzapfel, G.A., Gasser, T.C., Ogden, R.W., 2000. A new constitutive framework for arterial wall mechanics and a comparative study of material models. Journal of Elasticity 61 (1), 1–48.

Holzapfel, G.A., Sommer, G., Gasser, C.T., Regitnig, P., 2005a. Determination of layer-specific mechanical properties of human coronary arteries with nonatherosclerotic intimal thickening and related constitutive modeling. American Journal of Physiology—Heart and Circulatory Physiology 289 (5), H2048.

Holzapfel, G.A., Weizsäcker, H.W., 1998. Biomechanical behavior of the arterial wall and its numerical characterization. Computers in Biology and Medicine 28 (4), 377–392.

Huang, X., Yang, C., Yuan, C., Liu, F., Canton, G., Zheng, J., Woodard, P.K., Sicard, G.A., Tang, D., 2009. Patient-specific artery shrinkage and 3D zero-stress state in multi-component 3D FSI models for carotid atherosclerotic plaques based on in vivo MRI data. Molecular and Cellular Biomechanics: MCB 6 (2), 121.

Humphrey, J., Yin, F., 1987. A new constitutive formulation for characterizing the mechanical behavior of soft tissues. Biophysical Journal 52 (4), 563–570.

Karimi, R., Zhu, T., Bouma, B.E., Kaazempur Mofrad, M.R., 2008. Estimation of nonlinear mechanical properties of vascular tissues via elastography. Cardiovascular Engineering 8 (4), 191–202.

Kauer, M., Vuskovic, V., Dual, J., Szekely, G., Bajka, M., 2002. Inverse finite element characterization of soft tissues. Medical Image Analysis 6 (3), 275–287.

Kroon, M., 2010. A numerical framework for material characterisation of inhomogeneous hyperelastic membranes by inverse analysis. Journal of Computational and Applied Mathematics 234 (2), 563–578.

Lee, T., Garlapati, R.R., Lam, K., Lee, P.V.S., Chung, Y.S., Choi, J.B., Vincent, T.B.C., De, S.D., 2010. Fast tool for evaluation of iliac crest tissue elastic properties using the reduced-basis methods. Journal of Biomechanical Engineering 132, 121009.

Lei, F., Szeri, A., 2007. Inverse analysis of constitutive models: biological soft tissues. Journal of Biomechanics 40 (4), 936–940.

Li, J., Cui, Y., English, R., Alison Noble, J., 2009. Ultrasound estimation of breast tissue biomechanical properties using a similarity-based non-linear optimisation approach. The Journal of Strain Analysis for Engineering Design 44 (5), 363.

Li, W., Luo, X., Hill, N., Ogden, R., Smythe, A., Majeed, A., Bird, N., 2011a. A mechanical model for CCK-induced acalculous gallbladder pain. Annals of Biomedical Engineering 39 (2), 786–800.

Li, W., Luo, X., Hill, N., Ogden, R., Tian, T., Smythe, A., Majeed, A., Bird, N., 2011b. Cross-bridge apparent rate constants of human gallbladder smooth muscle. Journal of Muscle Research and Cell Motility 32 (3), 209–220.

Li, W., Luo, X., Hill, N., Smythe, A., Chin, S., Johnson, A., Bird, N., 2008. Correlation of mechanical factors and gallbladder pain. Computational and Mathematical Methods in Medicine 9 (1), 27.

Li, W.G., Luo, X.Y., Hill, N., Ogden, R., Smythe, A., Majeed, A., Bird, N., 2012. A quasi-nonlinear analysis on anisotropic behaviour of human gallbladder wall. Journal of Biomechanical Engineering 134 (10), 101009.

Liao, D., Duch, B., St½dkilde-J½rgensen, H., Zeng, Y., Gregersen, H., Kassab, G., 2004. Tension and stress calculations in a 3-D Fourier model of gall bladder geometry obtained from MR images. Annals of Biomedical Engineering 32 (5), 744–755.

Lu, J., Zhou, X., Raghavan, M.L., 2007a. Computational method of inverse elastostatics for anisotropic hyperelastic solids. International Journal for Numerical Methods in Engineering 69 (6), 1239–1261.

Lu, J., Zhou, X., Raghavan, M.L., 2007b. Inverse elastostatic stress analysis in pre-deformed biological structures: demonstration using abdominal aortic aneurysms. Journal of Biomechanics 40 (3), 693–696.

Luo, X.Y., Li, W.G., Bird, N., Chin, S.B., Hill, N.A., Johnson, A.G., 2007. On the mechanical behavior of the human biliary system. World Journal of Gastroenterology 13 (9), 1384–1392.

Mawe, G.M., 1998. Nerves and hormones interact to control gallbladder function. Physiology 13 (2), 84–90.

Merg, A.R., Kalinowski, S.E., Hinkhouse, M.M., Mitros, F.A., Ephgrave, K.S., Cullen, J.J., 2002. Mechanisms of impaired gallbladder contractile response in chronic acalculous cholecystitis. Journal of Gastrointestinal Surgery 6 (3), 432–437.

Michail, S., Preud'Homme, D., Christian, J., Nanagas, V., Goodwin, C., Hitch, D., Mezoff, A., 2001. Laparoscopic cholecystectomy: effective treatment for chronic abdominal pain in children with acalculous biliary pain. Journal of Pediatric Surgery 36 (9), 1394–1396.

Moré, J.J., Sorensen, D.C., 1983. Computing a trust region step. SIAM Journal on Scientific and Statistical Computing 4 (3), 553–572.

Moulton, M.J., Creswell, L.L., Actis, R.L., Myers, K.W., Vannier, M.W., Szabo, B.A., Pasque, M.K., 1995. An inverse approach to determining myocardial material properties. Journal of Biomechanics 28 (8), 935–948.

Parkman, H.P., Bogar, L.J., Bartula, L.L., Pagano, A.P., Thomas, R.M., Myers, S.I., 1999. Effect of experimental acalculous cholecystitis on gallbladder smooth muscle contractility. Digestive Diseases and Sciences 44 (11), 2235–2243.

Pauletzki, J., Sackmann, M., Holl, J., Paumgartner, G., 1996. Evaluation of gallbladder volume and emptying with a novel three-dimensional ultrasound system: comparison with the sum-of-cylinders and the ellipsoid methods. Journal of Clinical Ultrasound 24 (6), 277–285.

Raghavan, M., Ma, B., Fillinger, M.F., 2006. Non-invasive determination of zero-pressure geometry of arterial aneurysms. Annals of Biomedical Engineering 34 (9), 1414–1419.

Raghupathy, R., Barocas, V.H., 2010. Generalized anisotropic inverse mechanics for soft tissues. Journal of Biomechanical Engineering 132, 081006.

Ryan, J., Cohen, S., 1976. Gallbladder pressure–volume response to gastrointestinal hormones. American Journal of Physiology—Legacy Content 230 (6), 1461.

Samani, A., Plewes, D., 2007. An inverse problem solution for measuring the elastic modulus of intact ex vivo breast tissue tumours. Physics in Medicine and Biology 52, 1247.

Schulze-Bauer, C.A.J., Holzapfel, G., 2003. Determination of constitutive equations for human arteries from clinical data. Journal of Biomechanics 36 (2), 165–169.

Seshaiyer, P., Humphrey, J.D., 2003. A sub-domain inverse finite element characterization of hyperelastic membranes including soft tissues. Journal of Biomechanical Engineering 125, 363.

Smythe, A., Majeed, A., Fitzhenry, M., Johnson, A., 1998. A requiem for the cholecystokinin provocation test?. Gut 43 (4), 571.

Speelman, L., Bosboom, E.M.H., Schurink, G.W.H., Buth, J., Breeuwer, M., Jacobs, M.J., van de Vosse, F.N., 2009. Initial stress and nonlinear material behavior in patient-specific AAA wall stress analysis. Journal of Biomechanics 42 (11), 1713–1719.

Su, Y., 2005. The Mechanical Properties of Human Gallbladder. Department of Mechanical Engineering, Sheffield, University of Sheffield, UK. BEng: 66.

Tilleman, T.R., Tilleman, M.M., Neumann, M., 2004. The elastic properties of cancerous skin: Poisson's ratio and Young's modulus. The Israel Medical Association Journal: IMAJ 6 (12), 753.

Vavourakis, V., Papaharilaou, Y., Ekaterinaris, J., 2011. Coupled fluid–structure interaction hemodynamics in a zero-pressure state corrected arterial geometry. Journal of Biomechanics 44, 2453–2460.

Watton, P.N., Ventikos, Y., Holzapfel, G.A., 2009. Modelling the mechanical response of elastin for arterial tissue. Journal of Biomechanics 42 (9), 1320–1325.

Wegstapel, H., Bird, N., Chess-Williams, R., Johnson, A., 1999. The relationship between in vivo emptying of the gallbladder, biliary pain, and in vitro contractility of the gallbladder in patients with gallstones: is biliary colic muscular in origin?. Scandinavian Journal of Gastroenterology 34 (4), 421–425.

Westerhof, N., Lankhaar, J.W., Westerhof, B.E., 2009. The arterial windkessel. Medical and Biological Engineering and Computing 47 (2), 131–141.